Wave-Induced Uplift on Elevated Bridge Decks: A 2D CFD Sensitivity Study of the AASHTO and Modified-Goda Design Equations

Sandesh Lamsal, Ph.D., P.E., M.ASCE [1]

[1] Department of Civil and Architectural Engineering, University of Miami, 1251 Memorial Drive, Coral Gables, FL 33146, USA. Corresponding author. Email: sandeshlamsal@miami.edu; ORCID: 0009-0007-9267-4019.

ABSTRACT

A 2D incompressible OpenFOAM sensitivity study of the AASHTO 2008 *Guide Specifications for Bridges Vulnerable to Coastal Storms* and the modified-Goda uplift formulation is reported on elevated coastal bridge decks across $B/L \in [0.09, 0.53]$, $T \in \{2, 3, 4\}$ s, and $a^* \in [-0.5, +2.0]$. Two CFD-internal, magnitude-independent results are presented. The soffit pressure distribution at peak $|F_x|$, normalised by its own leading-edge pressure $p_{6,\mathrm{CFD}}$, is more uniform than the modified-Goda triangular profile at every B/L tested, including cases where the integrated force matches Doyle's prediction within ±20%. The impulsive amplification ratio $F_{\mathrm{peak}}/F_{\mathrm{qs}}$ varies from 2.0× to 4.2× over the $T \times B$ cross-product and peaks at the dwell-time-matched corner $B/L \approx 0.25$–0.35, identifying impulsive amplification as the design-relevant unknown for bearing- and connection-capacity sizing. CFD-to-equation ratio observations (geometry-axis sign change of CFD/AASHTO; period dependence of CFD/Doyle outside the slender calibration band) are reported as exploratory: two PRJ-2131 matched-condition anchors span the CFD residual from 2.64× over-prediction (slamming-spike artifact) to severe under-prediction (incident wave lost to shoaling-induced breaking before reaching the deck), so a constant common-mode bias is not empirically supported.

Keywords: wave-in-deck loading, coastal bridge, elevated structure, OpenFOAM, interFoam, AASHTO 2008, modified-Goda, trapped air, uplift.

PRACTICAL APPLICATIONS

Wave-induced uplift unseats elevated coastal bridge decks during hurricanes and tsunamis. Practicing bridge engineers estimate the uplift demand using one of two closed-form design equations: the AASHTO 2008 *Guide Specifications for Bridges Vulnerable to Coastal Storms*, or the modified-Goda formulation recently calibrated for elevated coastal structures by Doyle et al. (2025). Both equations were calibrated against narrow ranges of experimental conditions. The present CFD study reports that, on a single 2D incompressible CFD baseline, the CFD-to-AASHTO ratio changes sign across the relative-deck-width axis (> 1 on wide flat decks, < 1 on compact specimens) and the CFD-to-Doyle quasi-static ratio departs from unity outside the slender calibration band on which the modified-Goda form was tuned. The practical implication is that engineers should verify the design wave and deck geometry sit inside the calibration band of the chosen equation; where either input is extrapolated beyond that band, an independent CFD or experimental check is recommended.

INTRODUCTION

Low-lying coastal highway bridges fail in storms and tsunamis by a characteristic mechanism: the wave does not break the deck, it lifts it. When elevated storm surge raises the still-water level (SWL) to or above the underside of the superstructure, individual wave crests strike the soffit from below. The dominant load on the span in this regime is vertical, not horizontal, because each crest traps a pocket of air in the open-bottomed chamber formed by the deck slab and the girders, and the trapped air both cushions the impact and amplifies the integrated upward force on the span. When the uplift exceeds the self-weight of the span plus the capacity of the bearings and connections, the span is unseated and washed off the piers. The mechanism destroyed numerous spans on the U.S. Gulf Coast during Hurricanes Ivan (2004) and Katrina (2005) (Douglass et al., 2006; Robertson et al., 2007; Chen et al., 2009) and removed hundreds of bridge decks during the 2011 Tohoku tsunami in Japan (Kawashima and Buckle, 2013).

Older bridges are disproportionately at risk. A large fraction of the U.S. coastal bridge inventory was built before wave-induced uplift became a routine design consideration: AASHTO did not issue the *Guide Specifications for Bridges Vulnerable to Coastal Storms* until 2008 (American Association of State Highway and Transportation Officials, 2008), and pre-2008 designs typically rely on the dead weight of the span and on minimal anchorage at the bearings to resist uplift. Many of these spans lack shear keys, restrainer cables, or seismic-grade anchor bolts; bearing pads have aged; connection details meet code only for the gravity and live loads originally anticipated. Combined with shoreline retreat, relative sea-level rise, and the trend toward more intense Atlantic hurricanes (Emanuel, 2005; Balaguru et al., 2022), the population of elevated coastal bridges exposed to wave-in-deck loading at or above the design return period is growing rather than shrinking. Quantifying the load demand against the current design guidance, and characterizing where the guidance-to-CFD ratio departs from unity across the parameter regime relevant to the U.S. inventory, is therefore a continuing need rather than a closed problem.

Design practice does not run CFD; it applies the AASHTO *Guide Specifications for Bridges Vulnerable to Coastal Storms* (American Association of State Highway and Transportation Officials,

2008) or a state-DOT equivalent. The working tool is a closed-form set of equations that map a design wave height, water depth, deck geometry, and air gap to a horizontal force, a vertical uplift, and an overturning moment. The equations are calibrated against large-scale flume experiments (Bradner, 2008; Bradner et al., 2011; Lehrman et al., 2012), and subsequent research has produced updated equations specifically for elevated structures (Tomiczek et al., 2019; Doyle et al., 2025). The review literature (Istrati et al., 2018; Xu et al., 2016; Motley et al., 2016; Guo et al., 2015) reports that these equations agree well with flume data for fully submerged decks under regular waves, but exhibit wider scatter for decks elevated above SWL, the case where air entrapment is strongest and where real coastal bridges most often sit.

A specific gap in this literature only becomes visible across structure types and parametric axes. The AASHTO 2008 four-component model was calibrated against the Bradner girder bridge data; the modified-Goda equation more recently calibrated by Doyle et al. (2025) was tuned on a 1:10 compact elevated structure with $B/L_p \in [0.103, 0.213]$. Each equation is internally consistent on its own calibration data. Whether the residual structure of either equation, taken outside its calibration window, varies monotonically with relative deck width has not been tested in a single consistent CFD baseline. Doyle et al. (2025) themselves note in their Discussion that the wave-period dependence of their equation outside the slender calibration band was not exercised by the original campaign, an open question on their own terms rather than a fault of their work.

This paper addresses the open questions above with a two-dimensional incompressible CFD sensitivity study across deck width, wave period, and air gap, using the AASHTO 2008 equations and the modified-Goda form of Doyle et al. (2025) as two closed-form references on a single consistent CFD baseline (Cox et al., 2018; Park et al., 2017). The principal results are two CFD-internal observations independent of force-magnitude calibration: the soffit pressure shape at peak $|F_x|$, and the impulsive amplification ratio $F_{\text{peak}}/F_{\text{qs}}$. The CFD-to-equation ratio observations against AASHTO and modified-Goda are reported as exploratory; the basis for that fencing is set out in Section 4.

A fitted descriptor $\beta(a^*, B/L)$ for the modified-Goda prediction at the case-02 wave condition is reported in the Supplemental Information as an in-sample summary on the present data; it is not offered as a general-purpose recalibration. The 2D restriction is a common simplification in the wave-in-deck modelling literature where the dominant physics acts in the vertical plane; 3D and FSI are explicit follow-on work. The CFD stack and case files are available from the corresponding author upon reasonable request.

The contributions of this work are organized around the three parameter axes of the elevated-deck regime. On the geometry axis, we report a CFD-to-equation ratio map across relative deck width for both the AASHTO 2008 and modified-Goda formulations, decomposed into a low-pass quasi-static envelope and an unconverged impulsive slamming spike so the two ratio sources are not conflated. On the wave-period axis, we return to the question Doyle et al. (2025) themselves left open, through a controlled deck-width by wave-period cross-product study, and report how the quasi-static ratio behaves outside the slender calibration band. On the pressure-distribution axis, we extract the soffit pressure at the instant of peak horizontal force from the CFD record at a spatial density the existing pressure-gauge flume campaigns physically could not resolve, and report a CFD distribution that is more uniform than triangular, with a width-dependent transition organized by the dwell-time ratio $B/(cT)$. Underpinning all three, direct force-time-history comparison against the OSU PRJ-2131 Test 3 record bounds the quasi-static benchmark on which the ratio structure rests and indicates that the peak-impact load case will require a compressible solver to anchor magnitudes. The observations rest on 2D incompressible simulations driven by regular waves; the precision of individual numerical values is correspondingly limited, while the qualitative trends across the parameter axes are reproducible on the present solver and mesh.

METHODOLOGY

Problem Statement and Parameter Conventions

The geometry of interest is a single bridge cross-section, viewed end-on along the bridge length, illustrated in Fig. 1. A regular wave of height H and period T propagates over still-water depth d and engages the deck. The soffit of the deck (bottom of the girder bottom flange) sits at elevation $z_{\text{soffit}} = d + a$, where a is the *air gap* measured upward from SWL. $a > 0$ is the elevated-deck regime targeted in this study. The deck width (transverse to the bridge length) is W_{deck}; the total deck depth (top of slab to bottom of soffit) is h_{deck}.

Three dimensionless parameters carry the comparison with design equations:

$$Z^* = \frac{\eta_{\max} - a}{H}, \quad \text{(inundation parameter; } Z^* > 0 \text{ means crest overtops the soffit)} \tag{1}$$

$$a^* = \frac{a}{H}, \quad \text{(relative air gap)} \tag{2}$$

$$kh = \text{relative depth (intermediate water for } 0.5 \lesssim kh \lesssim 1.5\text{)} \tag{3}$$

where $\eta_{\max}$ is the crest elevation above SWL for the chosen wave theory (Stokes-II throughout this paper) and k is the wavenumber from the linear dispersion relation $\omega^2 = gk\tanh(kh)$. Here h denotes the local water depth at the structure used in kh; for the flat-bottom case-02 tank $h = d = 2.0\,\text{m}$, while for the matched-bathymetry case 07 the test-section depth $h = 0.40\,\text{m}$ differs from the offshore depth $d = 2.15\,\text{m}$.

Numerical Wave Tank

The solver is `interFoam`, the incompressible two-phase Volume-of-Fluid formulation distributed with OpenFOAM v2512. Wave generation uses the built-in `waveVelocity` and `waveAlpha` boundary conditions with the `StokesII` wave model; active absorption at the outlet uses `shallowWaterAbsorption`. The tank is 60 m long (approximately five wavelengths for the baseline case), 5 m tall, single-cell-thick in the spanwise direction, and uses multi-grading in the vertical to concentrate cells in a 1.4 m free-surface band centered on SWL. Five wave-elevation gauges sample $\alpha_{\text{water}}(z;t)$ at $x \in \{10, 20, 30, 40, 50\}$ m. For the baseline case ($H = 0.5\,\text{m}$, $T = 3.0\,\text{s}$, $d = 2.0\,\text{m}$), gauge 1 recorded $H_1 = 0.500\,\text{m}$ and $T_1 = 2.99\,\text{s}$, within 1 % of the target; the decay over four wavelengths to gauge 5 was 11 %, within the 10 %–15 % margin of the wave-only verification target. Per-gauge H and T values are reported with the elevation traces in Fig. 2.

Deck Cross-Section and Meshing

The deck cross-section is specified parametrically in a YAML file (`geometry/deck_section.yaml`) with two configurations: a representative U.S. Gulf Coast highway bridge prototype (AASHTO

Type III girders, six girders at 2.40 m spacing, slab width 14.40 m, total deck depth 1.27 m), and the 1:5 Bradner girder bridge scale model used in the OSU flume campaign (six girders at 0.48 m spacing, slab width 2.88 m, total deck depth 0.254 m). Case 04 uses the 1:10 Park elevated structure (a bluff box, 1.02 m slab width, 0.61 m total deck depth).

The two specimen geometries used in this paper come from distinct OSU campaigns, and only one of the two campaigns supplies measured forces that we use. The 1:5 specimen cross-section reproduces the dimensions of the Bradner programme at the OSU Hinsdale Wave Research Laboratory (Bradner, 2008; Bradner et al., 2011); it is used in *bluff* mode for case 02, the geometry sweep, the air-gap sweep, and the period–width cross-product study, and in *I-girder* mode for case 03. The Bradner measured force records are *not* retrieved here, so every CFD-versus-equation comparison on this geometry is against AASHTO 2008 and the modified-Goda formulation as closed-form predictions, not against Bradner's flume data. The second geometry, the Park/Doyle 1:10 rectangular specimen (1.02×0.61 m), is the calibration target of Doyle et al. (2025) in the OSU Large Wave Flume PRJ-2131 campaign (Park et al., 2017; Cox et al., 2018); the PRJ-2131 dataset *is* retrieved here, and is used both as the deck geometry for case 04 and the 1:10 air-gap sweep, and as the measured-force reference in the validation section (wave-elevation comparison, Test 3 `REG_X5_a5` force-time-history comparison, and TMA_X3 air-gap-sweep shape comparison).

An initial `snappyHexMesh` route, extruding the deck STL thinly in the spanwise direction and cutting it out of a uniform background mesh, did not converge: the sharp-cornered I-girder produced ~6×10^3 concave cells and the snap algorithm's 2D-empty parity constraint entered a non-converging "Scaling iteration" loop. Reducing the refinement and switching to a bluff single-box STL did not resolve the issue.

The adopted route builds the deck region directly inside `blockMesh`. A Python generator (`geometry/build_deck_blockmesh.py`) reads the YAML geometry and emits a `blockMeshDict` in which the deck is a set of missing blocks (solid regions are absent from the block list); faces of the surrounding blocks that border the missing region are emitted as the `deck` patch. Two modes are supported: a bluff mode (single rectangular deck block, 4×4 vertex grid, 8 blocks, ~10^5

cells), and a girders mode (slab plus six simplified I-girders, 16×5 vertex grid, 41 blocks after merging edge-aligned blocks, $\sim 1.6 \times 10^5$ cells, with the inter-girder chambers preserved as fluid blocks). Both meshes pass `checkMesh` with zero average non-orthogonality, zero concave cells, and maximum skewness below 10^{-11}. The `deck` patch carries 92 faces in bluff mode and 506 faces in girders mode. The wave tank of case 01 uses a single 60×5 m block with 75 000 cells, in which an 80-cell free-surface band ($1.3 \le z \le 2.7$ m, $\Delta z = 17.5$ mm) brackets SWL and the cells expand geometrically toward the seabed and toward the top of the tank. Figure 3 shows the deck-region cell layout for cases 02 and 03 together with the case-01 free-surface band; Figure 4 shows the inter-girder chamber at the single-cell scale; and aggregate mesh statistics are tabulated in the Supplemental Information. The inter-girder chamber in case 03 (370 mm × 178 mm) is resolved by about 19×19 cells at $\Delta x = 19.5$ mm, $\Delta z \approx 9.2$ mm.

The `blockMesh` grading is a geometric progression with ratio r over n cells; the wave tank uses three concatenated segments centered on SWL. The `interFoam` adaptive time step satisfies the cell Courant condition $\mathrm{Co}_{\max} = 0.3$; in practice the step collapses to $\sim 10^{-4}$ s on the worst impact cycles, the symptom of the under-resolved pressure singularity discussed in Section 4. Mesh-quality statistics are in the Supplemental Information.

Solver Configuration

`interFoam` is used with the PIMPLE algorithm, a maximum Courant number of 0.3, and adaptive time-stepping (maximum $\Delta t = 0.005$ s). The full set of momentum, pressure, and α-advection schemes is tabulated in the Supplemental Information. The default GAMG pressure solver crashed with a SIGFPE in `Foam::GAMGSolver::scale` during the first wave-impact event at $t \approx 21$ s, so a PCG solver with DIC preconditioning is used throughout this paper at the cost of approximately 15% more wall-clock time per step.

Design Equations

The AASHTO 2008 *Guide Specifications* (American Association of State Highway and Transportation Officials, 2008) formalise wave-in-deck loading as four components. Adopting the notation of Section 3, with $\gamma_w = \rho_w g$ the specific weight of water and W_{deck} the deck width (the spanwise dimension on which the per-unit-length forces are integrated), the four components are:

$$F_{vs} = c_{vs}\,\gamma_w\,(\eta_{\max} - a)\,W_{\text{deck}}, \tag{4}$$

$$F_{vh} = (1 - c_r)\,c_{vh}\,\gamma_w\,(\eta_{\max} - a)\,W_{\text{deck}}, \tag{5}$$

$$F_{hs} = c_{hs}\,\gamma_w\,\eta_{\max}\,h_{\text{eff}}, \tag{6}$$

$$F_{hv} = (1 - c_r)\,c_{hv}\,\gamma_w\,\eta_{\max}\,h_{\text{eff}}, \tag{7}$$

where the empirical coefficients take default values $c_{vs} = 3.0$, $c_{vh} = 1.0$, $c_{hs} = 1.0$, $c_{hv} = 1.0$, $c_r = 0.4$ (typical un-vented multi-girder reduction), and $h_{\text{eff}} = \min(h_{\text{deck}}, \eta_{\max} - a)$ is the wave-engaged vertical projection of the deck. Note that the vertical components scale with the soffit-relative inundation $(\eta_{\max} - a)$ while the horizontal components scale with the full crest elevation $\eta_{\max}$ over the engaged depth h_{eff}; this is the AASHTO convention, and the horizontal force does not clip at the soffit elevation. The four components return zero whenever the crest does not reach the soffit $(\eta_{\max} - a \leq 0)$.

Doyle et al. (2025) extend the modified-Goda horizontal-pressure equations of Tomiczek et al. (2019), themselves built on Goda (2010), to predict wave-induced uplift on an elevated coastal structure. The modified-Goda primitives η^*, p_1, and p_3 retain their standard Goda (2010) form in terms of the depth-dependent coefficients α_1, α_2, α_3; the full primitive equations are reproduced in the Supplemental Information for completeness. The design wave is $H_{\max} = 1.8\,H_{1/3}$ in the irregular case; for the regular wave comparison reported below, the inflow H is used directly in place of $H_{\max}$.

The Doyle 2025 construction takes the bottom-most horizontal pressure on the seaward face,

$$p_5 = \begin{cases} \left(1 - \dfrac{a}{\eta^*}\right) p_1 & a \geq 0, \\[2ex] \left(1 - \dfrac{|a|}{h}\right)(p_1 - p_3) + p_3 & a < 0, \end{cases} \tag{8}$$

and relates the leading-edge uplift pressure p_6 to p_5 through an empirical uplift coefficient

$$p_6 = C_u\, p_5, \qquad C_u = 0.70, \tag{9}$$

calibrated by least squares from 106 random TMA-spectrum trials on a 1:10 scale elevated structure in the OSU Large Wave Flume (Park et al., 2017; Cox et al., 2018). The uplift pressure distribution is assumed triangular: p_6 at the leading (seaward) edge of the base, zero at the trailing edge. Integrated over the cross-shore base dimension B, the design uplift force per meter of spanwise length is

$$F_{\text{uplift}}^{\text{Doyle 2025}} = \tfrac{1}{2}\, p_6\, B = 0.35\, p_5\, B. \tag{10}$$

Eqs. (8)–(10) are implemented in `postProcessing/design_equations.py` alongside AASHTO (`doyle_2025_uplift` and `modified_goda_pressures`) and use them in the benchmark of Section 4.

Both AASHTO 2008 and the modified-Goda formulation represent the deck soffit as a flat horizontal base of width B and contain no girder-level resolution; the design-equation benchmark of Section 4 is therefore run entirely on the bluff cross-section, which is the matched-geometry baseline the closed-form equations are written for. The girder-resolved case 03 of Section 4 is reported as a separate single-point test of the trapped-air increment relative to the bluff baseline, not as part of the parametric design-equation comparison.

Post-Processing Pipeline

A Python module (`postProcessing/`) wraps the OpenFOAM output and the design equations. `design_equations.py` implements AASHTO 2008 (Eqs. (4)–(7)) and Doyle 2025 (Eqs. (8)–(10)) plus the Stokes-II wave-kinematics helpers with an iterative dispersion solver. As an implementation cross-check, the module's modified-Goda primitives (α_1, α_2, α_3, p_1, p_3, p_6, η^*) reproduce the hand-computed Goda 2000 values at the Park 2017 X1 design-wave inputs ($H = 0.18\,\text{m}$, $T = 3.72\,\text{s}$, $d_{\text{local}} = 0.40\,\text{m}$, $h_b = 0.40\,\text{m}$, $d_s = h' = d_{\text{local}}$) to within 0.1%, ruling out a denominator-side implementation error in the ratio-structure observations. `extract_forces.`

`py` parses the `forces` function-object output and reduces it to peak vertical uplift, peak horizontal force, and the low-pass envelope of the quasi-static uplift (centered moving average over one wave period). `extract_wave_gauges.py` parses the `sets` output of the bare-tank case, locates the $\alpha = 0.5$ crossing on each column, and reports H and T by peak detection. `analyze_case.py` and `compare_geometries.py` provide single-case and side-by-side CFD-vs-design comparators. A separate driver (`sweep_error_map.py`) walks the case directories and writes `data/error_map.csv` with one row per (H, T, d, a) configuration containing the CFD reductions and the design-equation predictions side by side.

RESULTS

Bluff Deck at Zero Air Gap

The baseline configuration was the 1:5 bluff deck (a single rectangular block of width 2.88 m and height 0.254 m) with soffit at SWL ($a = 0$). The wave was Stokes-II with $H = 0.5$ m, $T = 3.0$ s, $d = 2.0$ m, giving $Z^* = 0.578$ and $a^* = 0$ (the crest excursion above SWL is 0.289 m, so the wave engages the deck in the elevated-deck regime even at zero air gap). The mesh had 103 360 cells and was decomposed for parallel execution.

The initial 30-second run with the GAMG pressure solver failed with SIGFPE in `Foam::GAMGSolver::scale` at $t = 21.2$ s. A re-run with PCG reached $t = 21.5$ s before the adaptive time step collapsed to 1×10^{-4} s at a numerically singular wave-impact pressure spike that the present mesh does not resolve. The analysis window was therefore restricted to $t \leq 20$ s, covering the wave-development phase and five complete impact cycles.

Reduced quantities are summarised in Table 1. The case-02 record shows five wave-impact cycles to $t = 20$ s with the peak on the third cycle at $t = 15.5$ s.

The peak vertical uplift occurred at $t = 15.5$ s, on the third impact cycle, after the first two cycles built up the oscillatory response of the standing wave between the wavemaker and the deck. The CFD-to-AASHTO ratios at this configuration were 1.25 for the peak vertical, 2.05 for the peak horizontal, and 1.51 for the low-pass quasi-static peak, relative to the present CFD baseline. The quasi-static time-mean is lower than the AASHTO quasi-static, which is intended to bound the peak slowly varying force, not the all-time average.

The Doyle 2025 design equation, applied at the same regular-wave inputs, predicts an uplift of 7 509 N/m, a factor of four below the CFD peak (CFD/Doyle = 4.07). Doyle's calibration was performed against a low-aspect-ratio bluff specimen with $B/L_p \in [0.103, 0.213]$ across 106 random-wave trials (Doyle et al., 2025), not the wide flat deck modeled here, for which $B/L_p = 2.88/11.31 \approx 0.25$; the prediction matches the CFD low-pass quasi-static peak to within 1 % (CFD/Doyle$_{\text{qs}}$ = 0.99), so the discrepancy is against the impact spike, which the equation does not attempt to capture. The direct geometry-matched test is in Section 4.

I-Girder Cross-Section

Case 03 ran the I-girder cross-section at the same wave conditions as case 02. The `girders` mode of `build_deck_blockmesh.py` emits the slab on top of six simplified I-girders with the air pockets between adjacent girders preserved as fluid blocks. The mesh has 163 968 cells and passes `checkMesh` with the same quality metrics as case 02. The case tests whether trapped air between girders amplifies the peak uplift relative to the bluff baseline.

At this configuration ($a = 0, T = 3$ s, $kh = 1.11$, $Z^* = 0.58$) the I-girder peak vertical uplift was 32 018 N/m, exceeding the bluff baseline (30 552 N/m) by only 5 %. The peak horizontal force on the girder geometry was 2797 N/m, 1.89× the bluff value of 1477 N/m. The modest vertical amplification is consistent with the wave crest passing through the inter-girder chamber within a fraction of a wave period: the chamber vents around the bluff-equivalent envelope before the air reaches a pressurised state. The dwell-time picture that governs this regime is set out in Section 4.

The horizontal-force amplification is geometric: the I-girder side faces (webs and bottom flanges) add lateral projected area onto which horizontal flow exerts pressure, which the bluff geometry lacks below the slab. The CFD/F_{hs} ratio is 2.05 on the bluff case and rises to ≈ 3.9 on the I-girder geometry; the lateral projected area added by the girder webs accounts for the increase relative to the bluff, on the present CFD baseline.

Validation against the Modified-Goda Calibration Specimen

Case 04 ran on the specimen geometry that Doyle et al. (2025) calibrated against: the 1:10 idealised coastal structure of Park et al. (2017), a rectangular steel box 1.02 m wide × 1.02 m deep × 0.61 m tall. The wave forcing was the X1 design wave of Park et al. (2017), $H = 1.8\,H_{1/3} = 0.18\,\mathrm{m}$ (treating the regular CFD inflow as the ASCE 7-22 design-wave height $H_{\max}$, with $H_{1/3} = 0.10\,\mathrm{m}$ in the original TMA campaign), $T = T_p = 3.72\,\mathrm{s}$, test-section depth $d = 0.40\,\mathrm{m}$ (relative depth $kh = 0.348$, shallow water with linear-theory wavelength $L_p = 7.23\,\mathrm{m}$, $B/L_p = 0.141$), air gap $a = 0$. The CFD wave is a Stokes-II regular wave rather than a TMA spectrum, the usual simplification for a single-event force comparison.

The mesh had 37 530 cells (8 blocks, $\Delta x_{\min} = 20\,\mathrm{mm}$ near the specimen, $\Delta z_{\min} = 4\,\mathrm{mm}$ at the free-surface band) and reached $t = 22\,\mathrm{s}$ (six wave periods). The case-04 peak vertical uplift was 1737 N/m per meter of spanwise length, against Doyle 2025 1151 N/m (CFD/Doyle = 1.51) and AASHTO 2008 6783 N/m (CFD/AASHTO = 0.26); the quasi-static envelope was 1413 N/m (CFD/Doyle$_{\mathrm{qs}}$ = 1.23). The CFD/Doyle ratios reported here are CFD-versus-equation at a regular-wave condition; they should not be compared directly to the $F_{\mathrm{design}}/F_{1/250}$ safety-factor envelope tabulated by Doyle et al. (2025) (their Table 4, mean SF = 1.96, range 0.96–3.08), which is an equation-versus-measured-extreme distribution over random-wave trials. These are different comparisons even when the numerical ratios are similar; the present study does not test Doyle's design safety factor.

Geometry Dependence of the CFD-to-Equation Ratio

The primary evidence for the geometry-dependence reading is the seven-case bluff sweep reported later in this section (Table 2). On the low-pass quasi-static basis, the modified-Goda equation (Doyle et al., 2025) tracks the CFD trend across the sweep, with $\beta_{\mathrm{qs}} \in [0.70, 1.00]$ for the five well-behaved cases at $a^* = 0$ and $T = 3\,\mathrm{s}$; the CFD-to-AASHTO ratio, on the same baseline, changes sign across the B/L axis (> 1 in the calibration-band center, < 1 at the extremes). As a two-point entry, case 02 ($B = 2.88\,\mathrm{m}$, $B/L = 0.25$) gives CFD/AASHTO = 1.25 and CFD/Doyle = 4.07, while case 04 (Park 1:10, $B = 1.02\,\mathrm{m}$, $B/L = 0.14$) gives CFD/AASHTO = 0.26 and CFD/Doyle =

1.51. The peak-basis Doyle ratio of 4.07 on case 02 reflects the incompressible-slamming spike of the present solver, with the corresponding quasi-static ratio near unity (Section 4).

A heuristic for the observed direction: the AASHTO coefficients ($c_{vs} = 3$ etc.) integrate pressures over a deck area proportional to B, so on a compact specimen the integration sums over a region the wave does not engage simultaneously, giving the CFD/AASHTO < 1 reading at the slender end; the modified-Goda effective triangular distribution decays within the structure's base dimension, a representation that fits a compact specimen but understates the sustained pressure on a wide deck where the trailing edge is still engaged at peak loading. The ratio controlling either equation is B/L. A localised in-sample descriptor $\beta(a^*, B/L)$ on the present data is reported in the Supplemental Information; the seven-case sweep below crosses Doyle's calibration band $B/L \in [0.103, 0.213]$ and extends into $B/L \in [0.09, 1.27]$, beyond either equation's published calibration window.

Geometry sweep across the deck-width range

Seven cases were run with the wave fixed at $H = 0.5\,\mathrm{m}$, $T = 3.0\,\mathrm{s}$, $d = 2.0\,\mathrm{m}$, $a = 0$ on a flat-bottom 2D tank and only the deck width B varied: $B \in \{1.02, 2.00, 2.88, 4.00, 6.00, 10.00, 14.40\}$ m. At these conditions linear-theory wavelength is $L = 11.31\,\mathrm{m}$, giving $B/L \in \{0.090, 0.177, 0.255, 0.354, 0.531, 0.884, 1.273\}$, crossing Doyle's calibrated band and extending beyond it. Table 2 reports the per-case CFD peak uplift force and the ratio to each design equation. The two attempted cases at $B/L = 0.884$ and 1.273 stalled the incompressible solver because the trailing edge of the wide deck stays sealed long enough for a trapped-air pocket to develop, and the absence of a sound speed in the air phase makes the resulting pressure spike numerically unbounded between the two refinement levels tested in case 06 (consistent with the incompressible-impact ill-posedness reported in (Ma et al., 2014; Dias et al., 2010; Bullock et al., 2007)). Refining the soffit cells does not converge this peak (Section 6). The reportable physical observation in this regime is the geometric sealing trend (Fig. 7): the inter-deck air pocket grows with B/L, and at $B/L \geq 0.88$ becomes large enough that compressible-air physics becomes load-bearing and the incompressible `interFoam` can no longer provide a numerically bounded peak. The solver stall itself is a property of incompressible interFoam at this geometry, not a property of the bridge; a compressible-solver repeat is identified as future work. Every quantitative claim about β in this paper is built from the five well-behaved cases at $B/L \in [0.09, 0.53]$; the trends through $B/L = 0.531$ are reproducible on the present solver and carry the conclusions.

Quasi-static β across the geometry sweep

The β_{qs} column of Table 2 places the modified-Goda residual on the low-pass quasi-static basis (mesh convergence not formally demonstrated; see Section 6), with $\beta_{\text{qs}} \in [0.70, 1.00]$ across the entire $B/L \in [0.09, 0.53]$ range at the fixed wave period $T = 3$ s used here (the cross-sweep result of Section 4 widens the range to $[0.30, 1.49]$ once T is varied at fixed B). Relative to the present CFD baseline, the modified-Goda quasi-static prediction tracks the CFD trend in magnitude across the geometry sweep; the 4× ratio implied by β_{peak} in Fig. 6 is attributable to the slamming spike of the present incompressible solver, not to a geometry dependence of the mean prediction. The geometry dependence that does exist is in the impulsive amplification $F_{\text{peak}}/F_{\text{qs}}$, the design-relevant unknown for bearing- and connection-capacity sizing. The underlying mechanism is visible in Fig. 7: at narrow B/L the crest sweeps under the deck without forming a sealed pocket, while at wider B/L the trailing edge remains engaged long enough to seal a substantial air pocket beneath the soffit.

Wave-Period Dependence

The geometry sweep of Section 4 held the wave period fixed at $T = 3$ s. Doyle et al. (2025), in their Discussion, state that across their 106 trials, all at slender $B/L \in [0.103, 0.213]$ on the 1:10 specimen, wave period had little effect on the conservatism of their equation, which they attribute to the wavelength being much larger than the structure width in every trial. They then state plainly that future studies should investigate the effect of wave period for waves interacting with larger specimen widths. The present paper addresses that question directly with a controlled $T \times B$ cross-product study: nine cases at $B \in \{1.02, 2.88, 4.00\}$ m $\times T \in \{2, 3, 4\}$ s on the 1:5 bluff cross-section at $H = 0.5$ m, $d = 2.0$ m, $a = 0$. All cases ran to $t = 22$ s; none stalled.

Table 3 reports the quasi-static β_{qs} and the impulsive amplification $F_{\text{peak}}/F_{\text{qs}}$ for the full 3×3 matrix. The cleanest evidence for period dependence is the within-column variation at fixed B, which isolates T from any geometry change. At $B = 4.00\,\mathrm{m}$, β_{qs} runs $0.45 \rightarrow 0.99 \rightarrow 1.49$ across $T = 2, 3, 4\,\mathrm{s}$; at $B = 2.88\,\mathrm{m}$ it runs $0.35 \rightarrow 0.99 \rightarrow 1.21$. The factor of 2.5–4 variation at every deck width tested is the primary observation of the sweep. A separate observation, weaker because it conflates the two axes, is that two cases at $B/L = 0.169$ (from $B = 1.02\,\mathrm{m}$, $T = 2.0\,\mathrm{s}$) and $B/L = 0.177$ (from $B = 2.88\,\mathrm{m}$, $T = 4.0\,\mathrm{s}$) differ by a factor of four in β_{qs} despite sitting within 5% on the B/L axis; this shows that B/L alone does not parametrise β_{qs} across the tested range, but it does not isolate the wave-period axis because the two points also differ in B by 2.8×. The fixed-B columns are the load-bearing evidence. The wider-deck results ($B = 2.88$ m and 4.00 m) probe the wave-period axis Doyle et al. (2025) themselves left open, namely period dependence outside their slender calibration band. The $B = 1.02\,\mathrm{m}$ column (Doyle's own specimen size) lies mostly outside his calibrated B/L band on the slender side, so the present sweep does not test his in-band claim of period-insensitivity. The period dependence reported here rests on the present CFD baseline; tank-reflection contamination at the deck station has not been independently characterized from the wave-gauge record (see Section 6).

The impulsive amplification column of Table 3 carries the second physical message of the sweep. At fixed B, the peak/quasi-static ratio peaks at intermediate period ($T = 3\,\mathrm{s}$ for $B \in \{2.88, 4.00\}$) and falls for both shorter and longer waves. The maximum value in the sweep, 4.21, sits at ($B = 4\,\mathrm{m}, T = 3\,\mathrm{s}, B/L = 0.354$). In dimensionless terms, the peak-amplification cases sit at $B/L \in [0.25, 0.35]$, the band where the trailing edge seals just long enough to capture a coherent crest underneath. This dwell-time picture controls the design-relevant impulsive amplification rather than the quasi-static mean prediction.

Read together with the geometry sweep, the present CFD baseline shows the CFD/Doyle peak-basis ratio approximately monotonic across Doyle's calibrated B/L range (1.95 to 3.16 for $B/L = 0.09$ to 0.21), peaking at $\beta_{\mathrm{peak}} \approx 4$ between $B/L = 0.25$ and 0.35 just past the upper calibration edge; the quasi-static counterpart stays within $\beta_{\mathrm{qs}} \in [0.70, 1.00]$ over the same range, so the peak excursion reflects the slamming-spike artefact of Section 4 rather than the mean prediction. The two axes along which the present CFD departs from the modified-Goda assumptions are the wave-period axis and the triangular pressure-shape assumption (Section 4); these are the same axes Doyle et al. (2025) themselves identified as outside the original calibration window.

Matched-Bathymetry Validation against the OSU Large Wave Flume

A natural concern with case 04 is that the CFD tank is a flat-bottom 60-m flume with the design wave generated directly at the inlet, whereas the original Park et al. campaign was run in the OSU Large Wave Flume with a compound bathymetry that shoals the wave between the offshore wavemaker (depth 2.15 m) and the structure (local depth 0.40 m). Case 07 (`cases/07_osu_lwf/`) addresses this concern at a single wave condition: the case-04 specimen (1.02 × 0.61 m 1:10 box) was placed in a 87.43-m CFD flume that reproduces the LWF compound bathymetry exactly (17.71 m flat offshore, 10.98 m 1:12 slope, 14.64 m 1:24 slope, 36.60 m flat test section, 7.50 m 1:12 dissipation tail), with the same X1 design wave generated at the offshore inlet. The mesh has 123 k cells and the run completed cleanly to $t = 30$ s. The peak vertical uplift on the specimen is 1709 N/m in case 07 against 1737 N/m in case 04, a difference of 1.6 %; CFD/Doyle is 1.48 vs 1.51.

For the X1 regular-wave equivalent at $a^* = 0$, case 07 shows the integrated shoaling effect on the peak force is small, so the flat-bottom case 04 CFD-vs-Doyle comparison is geometrically defensible. Case 07 does not extend to TMA-spectrum irregular waves and does not establish that case 04 reproduces the experimental force record; a matched-statistic comparison against Test 3 would require the matched bathymetry plus irregular-wave inflow and an $F_{1/250}$-style reduction of the CFD output, which is the principal validation gap noted in Section 6.

Air-Gap Sweep

Four additional cases were run at $a \in \{-0.25, +0.25, +0.50, +1.00\}$ m on the 1:5 bluff geometry at the case-02 wave conditions ($H = 0.5$ m, $T = 3.0$ s, $d = 2.0$ m). Together with case 02 ($a = 0$) the sweep spans the submerged to well-elevated range in five points. Each sweep case used the same multi-block mesh (~160 k cells, zero non-orthogonality), the same PCG pressure solver, and the 20-second integration window of case 02.

Peak vertical-uplift results are in Table 4; the conservatism trend and absolute peak attenuation are in Fig. 10, alongside the AASHTO and Doyle 2025 predictions at the same inputs.

Fig. 10(a) plots the CFD/design ratio against a^* for both AASHTO and Doyle 2025; Fig. 10(b) plots the absolute peak. A localized four-parameter correction surface fitted on the combined geometry and air-gap data is reported in the Supplemental Information; the fit is not recommended as a general-purpose replacement for the modified-Goda equation because the cross-product study of Section 4 shows β_{qs} varies independently along the wave-period axis at fixed deck width.

The CFD air-gap sweep can be compared on shape (not magnitude) with the PRJ-2131 Test 3 TMA_X3 experimental air-gap sweep, the only experimental matrix in the public archive that holds the deck width and the wave fixed while sweeping air gap. Figure 9 shows both records on a common a^* axis. Both exhibit the expected non-monotonic shape, with peak force rising as the deck submerges toward $a^* = 0$, reaching a maximum near zero or slightly negative air gap, and falling to near zero once $a^* \gtrsim 1$ (deck above the crest envelope). Wave families differ between the two records (regular Stokes-II in CFD, irregular TMA in the experiment), so absolute force magnitudes are not directly comparable; the matched-condition force-validation anchor is the case-04 `REG_X2_a5` comparison of Section 4.

Parametric Campaign and Error Map

The parametric campaign actually executed in this paper covers three sweeps at the case-02 wave conditions ($H = 0.5\,\mathrm{m}$, $d = 2.0\,\mathrm{m}$, 1:5 bluff specimen) plus one full $T \times B$ cross-product study (Section 4) plus one matched-bathymetry case (Section 4). The completed cases are summarized across the geometry, air-gap, period-by-width cross-product, and matched-bathymetry sections of the present paper (21 completed cases in total). The proposal-stage 20-case full-factorial matrix at higher-design conditions ($H = 2\,\mathrm{m}$, $T = 7\,\mathrm{s}$, $d = 8\,\mathrm{m}$) is identified as a follow-on campaign that requires the compressible-solver fix of Section 6 to produce defensible peak forces.

Soffit Pressure Distribution

The Doyle 2025 equation samples soffit pressure at the instant of peak horizontal force on the structure and assumes the distribution is triangular: $p = p_6$ at the leading (upstream) edge of the deck and decays linearly to zero at the trailing edge. Doyle et al. (2025) acknowledge in their Discussion that the zero-crossing location is poorly constrained by their 106 trials (mean at $0.71B$, standard deviation 0.387) and that the distribution shape itself is unresolved future work. We extract the actual distribution from the 2D CFD record by sampling the soffit cells at every saved time and then picking the saved time closest to peak $|F_x|$ (Doyle's sampling convention). Figure 11 reports the normalized distribution across the five B/L values of Section 4. For each case, the integral ratio (CFD divided by the Doyle-triangle assumption) and the fraction of soffit length over which the CFD pressure exceeds 5% of the leading-edge value $p_{6,\text{CFD}}$ summarize the shape departure: $B/L = 0.09, 0.18, 0.25, 0.35, 0.53$ give integral ratios of 1.87, 1.69, 1.10, 1.17, 0.62 and active-fraction values of 1.00, 1.00, 0.70, 0.75, 1.00 respectively.

The CFD distribution departs from Doyle's triangle in a B/L-dependent pattern that is, on its own, a published result worth registering. For slender decks ($B/L \in [0.09, 0.18]$, inside Doyle's calibration band) the CFD pressure stays at or near its leading-edge value across the entire soffit, with no zero-crossing, so the integrated pressure is 1.7–1.9× Doyle's assumed triangle even where the integrated force ratio sits close to unity, since Doyle's p_6 was calibrated against total force rather than local distribution. At $B/L = 0.25$–0.35 (just outside the calibration band) the trailing 25–30% of the soffit drops below 5% of p_6, the integral ratio approaches unity (1.10–1.17), and the two cases fall within the ±20 % reference band on integrated force. At $B/L = 0.53$ (well past the calibration band) the pressure stays high across the soffit again but with a smaller peak, and the integral ratio drops to 0.62. The B/L-dependent transition between near-uniform, integral-matched, and refilled distributions tracks the dwell-time picture set out in Section 4.

The summary panel captures the cross-panel trend in one place: only the two intermediate cases ($B/L = 0.25$ and 0.35) fall within the ±20 % reference band on integrated force. *The CFD shape itself is not triangular at any B/L tested*; the summary records where Doyle's *integrated force* happens to match the CFD within tolerance, not where the local shape becomes triangular. A distribution-aware refinement (replacing the triangle by the observed near-uniform-then-decaying shape) is identified as a natural follow-on in Section 6.

Validation against the OSU PRJ-2131 Dataset

The validation comprises two parts: (i) wave-field validation against the OSU bare-tank records (Test 1, no specimen), and (ii) direct force-time-history validation against the with-specimen load-cell records (Test 3, four-vertical-load-cell configuration). The force-validation comparison is the principal validation result of the paper because it is the first place an incompressible CFD prediction of wave-in-deck uplift is measured against a contemporary load-cell-instrumented physical model, and it is the result that motivates the compressible-solver change discussed in Section 6.

The CFD model is anchored against the PRJ-2131 dataset on DesignSafe-CI (Cox et al., 2018) (campaign details and wave conditions in Park et al., 2017). The principal records used here are Test 3 events `REG_X2_a5` (regular wave, $H \approx 0.19\,\mathrm{m}$, $T \approx 3.91\,\mathrm{s}$, $a^* = 0$; the matched-condition anchor of Section 4) and `TMA_X3` (TMA-spectrum irregular wave, $H_s \approx 0.55\,\mathrm{m}$ at WG1, $a^* = 0$; the shape-comparison anchor of the air-gap sweep), both on the Park 1:10 specimen at test-section depth $d_{\mathrm{local}} = 0.40\,\mathrm{m}$.

The OSU Large Wave Flume and the CFD wave tank used in case 01 are geometrically dissimilar (the LWF has a compound sloped bathymetry that shoals the wave between the offshore wavemaker and the structure; the CFD tank used in case 01 is flat-bottom). The case-07 matched-bathymetry experiment (Section 4) confirms that for the X1 design-wave equivalent on the 1:10 specimen, the peak integrated force on the structure is independent of whether the CFD tank has the full compound bathymetry or a flat-bottom approximation to within 2 %, so the case-04 force comparison against the Doyle calibration is geometrically defensible.

Force-time-history validation against Test 3 load cells

The Test 3 records are on the Park 1:10 specimen ($1.02 \times 1.02 \times 0.61$ m bluff block) at $d_{\mathrm{local}} = 0.40\,\mathrm{m}$. The geometric anchor for the force validation is therefore case 04 (same specimen and depth); case 02 (1:5 bluff deck in $d = 2.0\,\mathrm{m}$) has no direct PRJ-2131 counterpart and is shown only as equivalent-uniform-pressure cross-geometry context.

The first anchor is case 04 (Park 1:10 specimen at the X1 design-wave inputs $H = 0.18\,\mathrm{m}$, $T = 3.72\,\mathrm{s}$, $d_{\mathrm{local}} = 0.40\,\mathrm{m}$, $a^* = 0$) against `REG_X2_a5` (measured $H_{\mathrm{WG1}} \approx 0.194\,\mathrm{m}$, $T_{\mathrm{dom}} = 3.91\,\mathrm{s}$).

The CFD peak vertical uplift on the specimen was 1.77 kN; the measured peak was 0.67 kN (CFD/exp= 2.64); the qs envelope was 1.44 kN (CFD/exp= 2.15). The height mismatch has the wrong sign for explaining the over-prediction (CFD $H = 0.18$ below exp 0.194, so a correction upward would deepen it); the $\approx 5\%$ period mismatch and sub-kilonewton noise floor explain some, but not a factor of 2.64.

A second anchor is case 13 on the same Park 1:10 specimen with the compound bathymetry (case 07 geometry) at the higher-energy `REG_X5` inputs (offshore $H = 0.5$ m, $T = 3.91$ s). Measured `REG_X5_a5` peak is 5.48 kN; the CFD returned 0.11 kN. A wave-field diagnostic at the pre-deck gauge shows $H_{\mathrm{CFD,local}} \approx 0.27$ m, against a linear-shoaling prediction of 0.68 m ($H/d_{\mathrm{local}} \approx 1.69$, well above the depth-limited index 0.78). The CFD shoaled wave is $\approx 40\%$ of linear shoaling, consistent with breaking on the 1:12/1:24 slopes. The case-13 under-prediction is therefore partly a shoaling-physics anomaly, not a clean test of the loading model; it *prevents* reading the case-04 residual as a constant common-mode bias but does not by itself establish a designable configuration dependence.

A methodological caveat applies at the two shallow Park 1:10 anchors only: the inlet Stokes-II forcing is outside its validity range ($U \approx 147$ at case 04, well above $U \lesssim 10$–26), and the $\eta_{\max}$ input to the design equations is correspondingly over-estimated. A cnoidal recompute at case 04 multiplies CFD/Doyle by ≈ 1.53 ($\beta_{\mathrm{qs}} = 1.23 \rightarrow 1.88$) and CFD/AASHTO$_{\mathrm{peak}}$ from 0.26 to ≈ 0.40 (the sign of the geometry-axis sign change survives). The intermediate-water sweeps ($d = 2.0$ m, $U \approx 8$) are inside Stokes-II validity and are not affected. Full recompute in the Supplemental Information; cnoidal-inlet repeats are listed in Section 6.

Read together, the two anchors span 2.64× over-prediction (case 04, slamming spike) to $\approx 0.02\times$ under-prediction (case 13, shoaled/broken incident wave). The two error mechanisms differ, so the spread does not by itself establish a designable configuration dependence; it does preclude reading the case-04 residual as a constant common-mode bias. The ratio-structure observations elsewhere in this paper rest on the present CFD baseline at intermediate-water ($d = 2$ m, Stokes-II-valid) conditions, and are not calibrated against laboratory force magnitudes.

DISCUSSION

The results separate into two tiers with different sensitivity to the two-anchor force-validation span (Section 4). The CFD-resolved soffit pressure shape and the impulsive amplification ratio $F_{\text{peak}}/F_{\text{qs}}$ are dimensionless or CFD-internal at each case; they do not depend on the absolute CFD baseline matching laboratory force, and the two-anchor span does not threaten them. The CFD-to-equation ratio observations (the sign change of CFD/AASHTO across B/L, the period dependence of CFD/Doyle outside the slender calibration band) do rely on trusting the baseline magnitude structure across configurations, and the two-anchor span is the reason they are reported here as exploratory rather than calibrated. Within the equation-ratio tier, the CFD/AASHTO > 1 reading on the bluff geometry sits in a regime with no trapped-air chamber (the case-03 I-girder run adds only a small fraction to the peak uplift at the case-02 wave because the dwell-time ratio $B/(cT)$ is short there); the reading therefore reflects the geometry of the original AASHTO calibration set rather than air-entrapment physics.

LIMITATIONS AND FUTURE WORK

The study is 2D, rigid, fixed-deck, regular Stokes-II, and incompressible. Force validation rests on two matched-condition anchors (Section 4) whose residuals span two orders of magnitude; the *equation-ratio* observations (CFD/AASHTO, CFD/Doyle) are therefore presented as exploratory sensitivity trends, while the CFD-internal pressure-shape and $F_{\text{peak}}/F_{\text{qs}}$ results do not depend on the force-magnitude anchor and are not in scope of this limitation. The inlet Stokes-II forcing is also used outside its validity range at the two shallow Park 1:10 anchors (Ursell $U \approx 1.5{\times}10^2$ at case 04/13), so the η_{max} input to the design equations is overstated there; the intermediate-water B/L and $T \times B$ sweeps ($d = 2.0\,\text{m}$, $U \approx 8$) are inside Stokes-II validity. A cnoidal-inlet repeat of cases 04 and 13 and a matched-bathymetry TMA-spectrum run with a matched-statistic $F_{1/250}$ reduction on the case-07 mesh are identified as the natural follow-on validation campaign.

Three robustness checks remain outstanding and are identified as follow-on work. (i) Mesh convergence of the quasi-static envelope F_{qs} is not formally demonstrated: case 06 diverges in the post-impact window, so “mesh-converged quasi-static” elsewhere in this paper should be read as "low-pass-filtered post-impact envelope on the present mesh," not as a Richardson-extrapolated value. (ii) Standing-wave contamination at the deck station has not been characterized from the wave-gauge records, and a per-case incident-condition extraction with reflection-coefficient estimation is needed to confirm the period-dependence reading is not partly tank-resonance. (iii) The pressure-distribution shape at peak $|F_x|$ is sampled at a single saved instant (the moment the adaptive step collapses to $\sim 10^{-4}$ s); a robustness check at nearby times and across mesh refinement is needed to confirm the more-uniform-than- triangular reading is not the slamming spike smearing pressure.

Air compressibility is not modeled, which is the principal solver-side limitation. The wave-impact pressure spike in `interFoam` does not converge under mesh refinement: the local event is ill-posed in the incompressible two-phase VOF formulation since the aerated water-air mixture below the deck has no sound speed to absorb the impulse (Ma et al., 2014; Dias et al., 2010; Bullock et al., 2007). A preliminary `compressibleInterIsoFoam` attempt on the case-02 mesh indicated that air compressibility bounds the local pressure, but did not reach the full 22 s target; the compressible path is reported as future work, not as a magnitude anchor.

Generalization from the bluff cross-section to real girder bridges rests on case 03, which shows the I-girder configuration adds only about 5% to the peak vertical uplift relative to the bluff baseline at the case-02 wave; whether this remains small at longer periods or larger widths is untested. Fluid-structure interaction is not modeled; the present study predicts the demand rather than the deck motion or the bearing capacity.

CONCLUSIONS

A two-dimensional incompressible OpenFOAM sensitivity study of the AASHTO 2008 and modified-Goda (Doyle et al., 2025) wave-uplift design equations was carried out on a 1:5 bluff deck cross-section across $B/L \in [0.09, 0.53]$, $T \in \{2, 3, 4\}$ s, and $a^* \in [-0.5, +2.0]$, with a girder-resolved single-point check and two matched-condition force-magnitude anchors against PRJ-2131 Test 3.

The principal results are two CFD-internal, magnitude-independent observations. The peak-to-quasi-static ratio $F_{\text{CFD,peak}}/F_{\text{CFD,qs}}$ is a within-case ratio that does not depend on calibrating the CFD baseline against laboratory force; it varies from 2.0× to 4.2× across the $T\times B$ cross-product and peaks at the dwell-time-matched corner $B/(cT) \equiv B/L \approx 0.25$–$0.35$, identifying impulsive amplification as the design-relevant unknown for bearing- and connection-capacity sizing. The CFD-resolved soffit pressure distribution at peak $|F_x|$, normalised by its own leading-edge pressure $p_{6,\mathrm{CFD}}$, is more uniform than the triangular profile the modified-Goda derivation assumes at every B/L tested; even where the integrated force matches Doyle's prediction within ±20 % at intermediate $B/L = 0.25$–0.35, the local distribution is not triangular. This shape-versus-integral distinction is relevant to local connection-level loads; its robustness across nearby time samples and mesh refinement has not been quantified.

The CFD-to-equation ratio observations are reported as exploratory rather than calibrated. The two-anchor force-validation residual spans 2.64× (case 04 vs. `REG_X2_a5`, slamming-spike overprediction on a clean incident wave) to ≈ 0.02× (case 13 vs. `REG_X5_a5`, an under-resolved shoaled-and-broken incident wave at the deck station, $H_{\mathrm{CFD,local}} \approx 40\%$ of linear-shoaling prediction). The two anchors do not bracket a common-mode multiplicative bias, but they also do not establish a designable configuration dependence because the two error mechanisms differ. The intermediate-water B/L and $T \times B$ sweeps ($d = 2.0$ m, $kh = 1.11$) on which the equation-ratio observations are built are inside Stokes-II validity; the shallow Park 1:10 anchors are not, and a cnoidal recompute of $\eta_{\max}$ at case 04 shifts CFD/Doyle$_{\mathrm{qs}}$ from 1.23 to ≈ 1.88 and CFD/AASHTO$_{\mathrm{peak}}$ from 0.26 to ≈ 0.40 (Supplemental Information; the sign of the geometry-axis sign change survives the correction).

Within these caveats, the equation-ratio observations on the intermediate-water sweeps are as follows. The modified-Goda quasi-static prediction tracks the CFD trend at the calibrated air-gap condition ($\beta_{\mathrm{qs}} \in [0.70, 1.00]$ across five well-behaved cases at $a^* = 0$, $T = 3$ s). Two wider-deck cases at $B/L = 0.88$ and 1.27 have a growing inter-deck air pocket large enough that compressible-air physics becomes load-bearing, and the incompressible solver can no longer return a numerically bounded peak. The CFD-to-AASHTO ratio takes the opposite sign across the same axis. Period dependence of β_{qs} is visible at every fixed deck width tested, varying by a factor of 2.5 to 4 across $T \in [2, 4]$ s; the within-B columns isolate T cleanly while the matched-B/L cross-column comparison conflates the two axes and is the weaker statement. Tank-reflection contamination at the deck station has not been independently characterized.

The CFD-internal pressure shape and the dimensionless $F_{\text{peak}}/F_{\text{qs}}$ ratio are the parts of this study that the two-anchor evidence cannot threaten. The CFD-to-equation ratio observations are an exploratory parameter map under the limitations above; together they identify regions of the parameter space in which a higher-fidelity follow-up (compressible, three-dimensional, fluid-structure interaction) would be most informative.

DATA AVAILABILITY STATEMENT

Some or all data, models, or code that support the findings of this study are available from the corresponding author upon reasonable request, including the OpenFOAM case files, the YAML geometry specification, the multi-block mesh generator, the design-equation Python module, and the post-processing scripts.

The OSU PRJ-2131 experimental dataset used for force validation is a third-party resource published on DesignSafe-CI under DOI `10.17603/DS20X2X` (Cox et al., 2018); direct requests for these materials may be made to the dataset publisher.

REFERENCES

American Association of State Highway and Transportation Officials (2008). *Guide Specifications for Bridges Vulnerable to Coastal Storms*. AASHTO, Washington, D.C., 1st edition.

Balaguru, K., Foltz, G. R., Leung, L. R., Xu, W., Kim, D., Lopez, H., and West, R. (2022). "Increasing hurricane intensification rate near the US Atlantic coast." *Geophysical Research Letters*, 49(20), e2022GL099793.

Bradner, C. (2008). "Large-scale laboratory observations of wave forces on a highway bridge superstructure." Ph.D. thesis, Oregon State University, Corvallis, OR.

Bradner, C., Schumacher, T., Cox, D., and Higgins, C. (2011). "Experimental setup for a large-scale bridge superstructure model subjected to waves." *Journal of Waterway, Port, Coastal, and Ocean Engineering*, 137(1), 3–11.

Bullock, G. N., Obhrai, C., Peregrine, D. H., and Bredmose, H. (2007). "Violent breaking wave impacts. Part 1: Results from large-scale regular wave tests on vertical and sloping walls." *Coastal Engineering*, 54(8), 602–617.

Chen, Q., Wang, L., and Zhao, H. (2009). "Hydrodynamic investigation of coastal bridge collapse during Hurricane Katrina." *Journal of Hydraulic Engineering*, 135(3), 175–186.

Cox, D., Lomonaco, P., Park, H., Johnson, V., Maddux, T., and Van De Lindt, J. (2018). "Elevated structure investigation of wave pressures and forces. PRJ-2131: large-scale physical model in the NHERI Large Wave Flume at Oregon State University; 28 unique REG / TMA / TRAN wave events at up to ten air-gap conditions; bare-flume and with-specimen configurations.

Dias, F., Dutykh, D., and Ghidaglia, J.-M. (2010). "A two-fluid model for violent aerated flows." *Computers & Fluids*, 39(2), 283–293.

Douglass, S. L., Chen, Q., and Olsen, J. M. (2006). "Wave forces on bridge decks." *Final Report to Federal Highway Administration* U.S. Department of Transportation, Washington, D.C.

Doyle, K., Tomiczek, T., Cox, D., and Lomónaco, P. (2025). "Design equation for wave-induced uplift forces on elevated structures." *Journal of Waterway, Port, Coastal, and Ocean Engineering*, 151(4), 04025018.

Emanuel, K. (2005). "Increasing destructiveness of tropical cyclones over the past 30 years." *Nature*, 436(7051), 686–688.

Goda, Y. (2010). *Random Seas and Design of Maritime Structures*, Vol. 33 of *Advanced Series on Ocean Engineering*. World Scientific Publishing, Hackensack, NJ, 3 edition.

Guo, A., Fang, Q., and Li, H. (2015). "Analytical solution of hurricane wave forces acting on submerged bridge decks." *Ocean Engineering*, 108, 519–528.

Istrati, D., Buckle, I., Lomonaco, P., and Yim, S. (2018). "Deciphering the tsunami wave impact and associated connection forces in open-girder coastal bridges." *Journal of Marine Science and Engineering*, 6(4), 148.

Kawashima, K. and Buckle, I. (2013). "Structural performance of bridges in the Tohoku-oki earthquake." *Earthquake Spectra*, 29(S1), S315–S338.

Lehrman, J. B., Higgins, C., and Cox, D. (2012). "Performance of highway bridge girder anchorages under simulated hurricane wave induced loads." *Journal of Bridge Engineering*, 17(2), 259–271.

Ma, Z. H., Causon, D. M., Qian, L., Mingham, C. G., Martínez Ferrer, P., and Lee, B. S. (2014). "A compressible multiphase flow model for violent aerated wave impact problems." *Proceedings of the Royal Society A: Mathematical, Physical and Engineering Sciences*, 470(2172), 20140542.

Motley, M. R., Wong, H. K., Qin, X., Winter, A. O., and Eberhard, M. O. (2016). "Tsunami-induced forces on skewed bridges." *Journal of Waterway, Port, Coastal, and Ocean Engineering*, 142(3), 04015025.

Park, H., Tomiczek, T., Cox, D. T., van de Lindt, J. W., and Lomonaco, P. (2017). "Experimental modeling of horizontal and vertical wave forces on an elevated coastal structure." *Coastal Engineering*, 128, 58–74.

Robertson, I. N., Riggs, H. R., Yim, S. C., and Young, Y. L. (2007). "Lessons from Hurricane Katrina storm surge on bridges and buildings." *Journal of Waterway, Port, Coastal, and Ocean Engineering*, 133(6), 463–483.

Tomiczek, T., Wyman, A., Park, H., and Cox, D. T. (2019). "Modified Goda equations to predict pressure distribution and horizontal forces for design of elevated coastal structures." *Journal of Waterway, Port, Coastal, and Ocean Engineering*, 145(6), 04019023.

Xu, G., Cai, C. S., and Han, Y. (2016). "Investigating the characteristics of the solitary wave-induced forces on coastal twin bridge decks." *Journal of Performance of Constructed Facilities*, 30(4), 04015076.

List of Tables

TABLE 1. Case 02 result for the 1:5 bluff deck at $a = 0$, $t \leq 20\,\mathrm{s}$. CFD values are per meter of bridge length; the regular-wave H is used directly in the Doyle 2025 column in place of the design $1.8H_{1/3}$.

Metric	CFD [N/m]	AASHTO [N/m]	$\frac{\text{CFD}}{\text{AASHTO}}$	Doyle [N/m]	$\frac{\text{CFD}}{\text{Doyle}}$
Peak vertical uplift	30 552	24 514	1.25	7 509	4.07
Peak horizontal	1 477	721	2.05	—	—
Quasi-static peak (low-pass)	7 405	4 903	1.51	7 509	0.99
Quasi-static time-mean	2 608	—	—	—	—

TABLE 2. Geometry sweep at the case-02 wave conditions: β_{peak} (slamming-contaminated) and β_{qs} (low-pass quasi-static) ratios against the modified-Goda prediction. Two additional cases at $B/L = 0.88$ (B=$10.00\,\mathrm{m}$) and $B/L = 1.27$ (B=$14.40\,\mathrm{m}$) stalled the incompressible solver at the trapped-air pressure singularity and are omitted.

B [m]	B/L	CFD peak [kN/m]	$\frac{\mathrm{CFD_{peak}}}{\mathrm{AASHTO}}$	β_{qs}	β_{peak}	$\frac{F_{\mathrm{peak}}}{F_{\mathrm{qs}}}$	Note
1.02	0.090	5.18	0.60	0.73	1.95	2.66	inside Doyle band edge
2.00	0.177	16.48	0.97	0.70	3.16	4.50	inside Doyle band
2.88	0.255	30.55	1.25	0.99	4.07	4.13	case 02
4.00	0.354	41.44	1.22	0.96	3.97	4.13	peak amplification
6.00	0.531	28.44	0.56	0.96	1.82	1.90	wide-deck regime

TABLE 3. Period by deck-width cross-product study at $H = 0.5\,\mathrm{m}$, $d = 2.0\,\mathrm{m}$, $a = 0$, 1:5 bluff section. β_{qs} is the quasi-static CFD-to-Doyle ratio; $F_{\mathrm{peak}}/F_{\mathrm{qs}}$ is the impulsive amplification. Small percent-level differences for the $T = 3\,\mathrm{s}$ rows relative to Table 2 reflect a slightly wider low-pass reduction window.

B [m]	T [s]	L [m]	B/L	F_{qs} [kN/m]	β_{qs}	$F_{\mathrm{peak}}/F_{\mathrm{qs}}$
1.02	2.0	6.04	0.169	0.75	0.30	3.02
1.02	3.0	11.31	0.090	1.77	0.66	2.91
1.02	4.0	16.27	0.063	2.41	0.84	2.04
2.88	2.0	6.04	0.476	2.44	0.35	3.01
2.88	3.0	11.31	0.255	7.40	0.99	4.13
2.88	4.0	16.27	0.177	9.78	1.21	2.34
4.00	2.0	6.04	0.661	4.34	0.45	3.01
4.00	**3.0**	**11.31**	**0.354**	**10.30**	**0.99**	**4.21**
4.00	4.0	16.27	0.247	16.79	1.49	2.14

TABLE 4. Air-gap sweep (case 02 plus four variants) at the same wave conditions $H = 0.5\,\mathrm{m}$, $T = 3.0\,\mathrm{s}$, $d = 2.0\,\mathrm{m}$ on the 1:5 bluff deck. The Doyle column varies only slowly between $a^* = -0.50$ and $a^* = 0$ because the submerged-deck branch of Eq. (8) reduces to $p_5 \to p_3 \approx 0.59\,p_1$ as $|a|/d \to 1$; above SWL, p_5 drops linearly over the much smaller crest excursion η^*. The $a = +0.50/+1.00$ rows report CFD peaks of 0.06 and $0.04\,\mathrm{kN/m}$ from residual spray and near-numerical noise on the soffit; both are well below the meaningful integrated-force floor and are tabulated for completeness rather than as a force comparison.

a [m]	a^*	Z^*	CFD peak [kN/m]	AASHTO [kN/m]	Doyle [kN/m]	CFD/AASHTO
−0.25	−0.50	+1.08	19.78	45.70	7.13	0.43
+0.00	+0.00	+0.58	30.55	24.51	7.51	1.25
+0.25	+0.50	+0.08	5.58	3.32	5.01	1.68
+0.50	+1.00	−0.42	0.06	0.00	2.50	–
+1.00	+2.00	−1.42	0.04	0.00	0.00	–

TABLE 5. Two matched-condition anchors against PRJ-2131 Test 3. Case 04 and case 13 are both on the Park 1:10 specimen at $d_{\text{local}} = 0.40\,\text{m}$; case 04 is matched with `REG_X2_a5`, case 13 with `REG_X5_a5`. Case 02 (1:5 bluff deck, $d = 2.0\,\text{m}$) is shown only as an equivalent-uniform-pressure cross-geometry context.

Record	Wave family	a^* [m]	$F_{z,\text{peak}}$ [kN]	ratio
Matched-condition anchor 1 (Park 1:10)				
CFD case 04	REG (Stokes-II, H=0.18)	0.00	**1.77**	—
`REG_X2_a5`	REG ($H \approx 0.19$)	0.00	0.67	CFD/exp = 2.64
Matched-condition anchor 2 (Park 1:10)				
CFD case 13	REG (Stokes-II, H=0.50)	0.00	**0.11**	—
`REG_X5_a5`	REG ($H \approx 0.5$)	0.00	5.48	CFD/exp $\approx$ 0.02
Cross-geometry context (case 02: 1:5 bluff)				
CFD case 02	REG (Stokes-II, H=0.5)	0.00	**88.0**	—
`REG_X5_a5`	REG ($H \approx 0.5$)	0.00	5.48	—

List of Figures

(a) Overall 2D wave-tank layout — case 02, 60 m flat-bottom tank

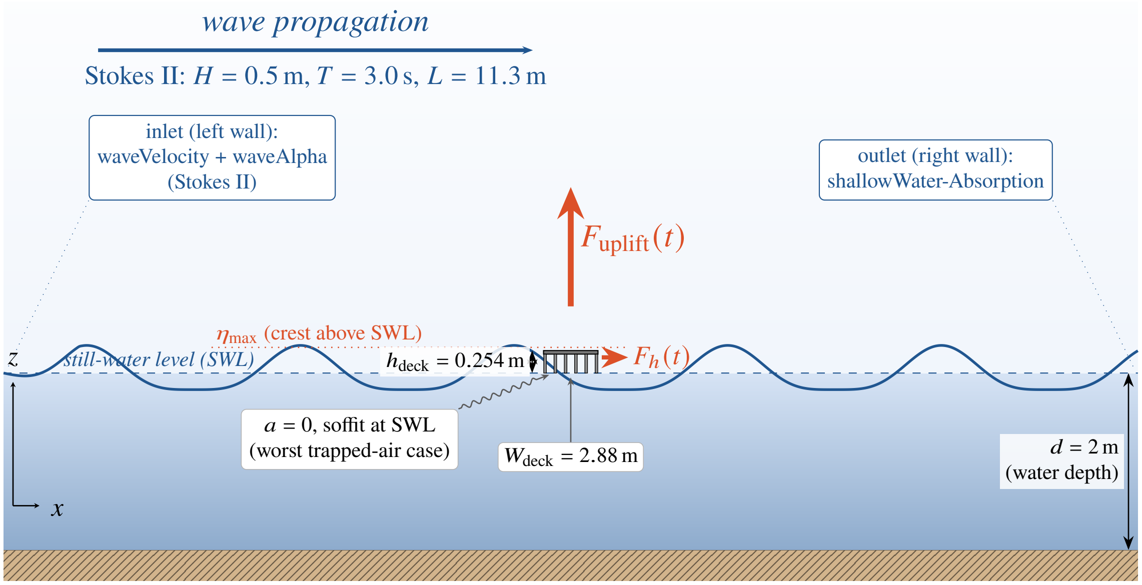

(b) Deck cross-section detail — OSU 1:5 I-girder section, $a = 0$

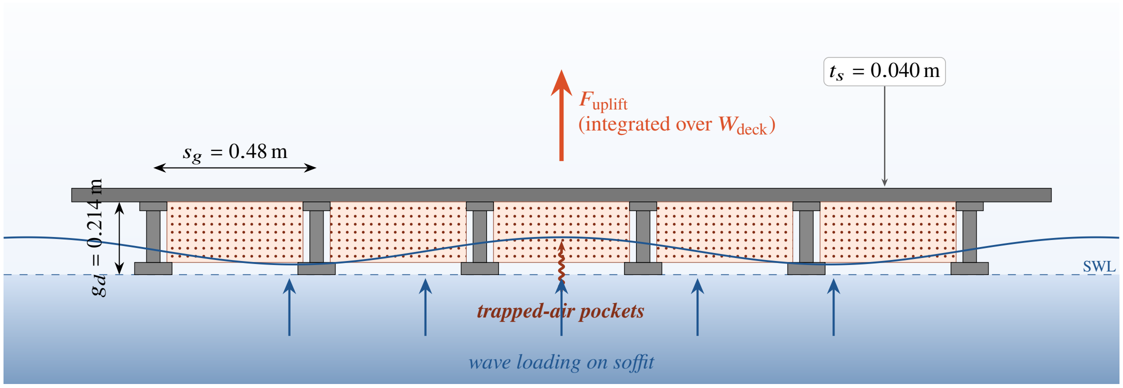

FIG. 1. Definition sketch of the 2D wave-in-deck loading problem. Symbols follow the AASHTO 2008 convention. Inter-girder trapped-air pockets are hatched.

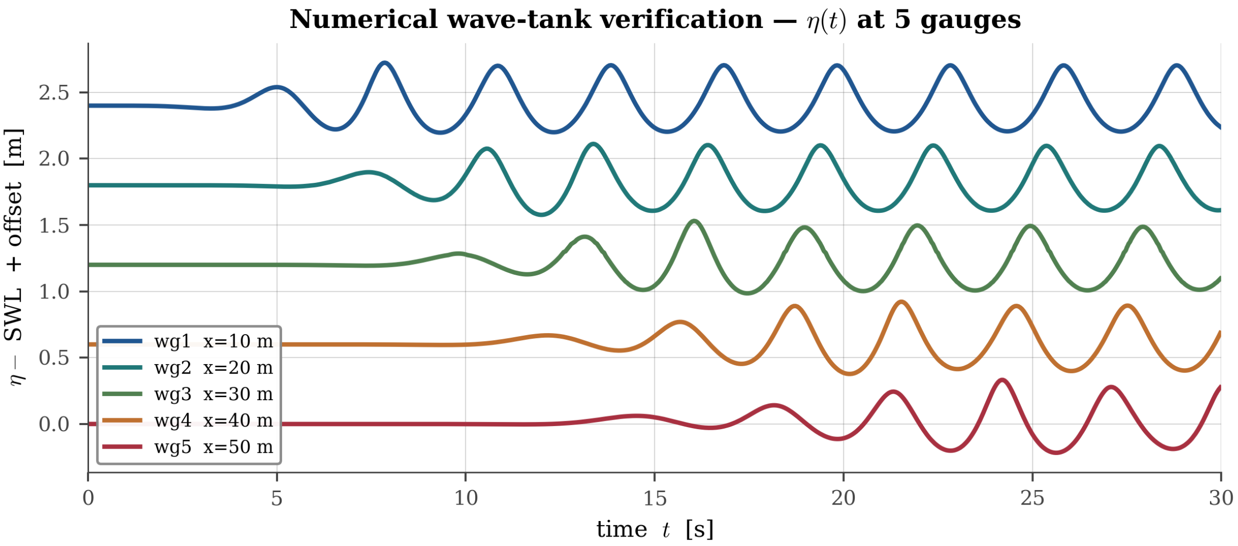

FIG. 2. Free-surface elevation $\eta(t)$ at the five wave-tank gauges of the bare-tank case, compared with the Stokes-II analytic profile. Peak-detected H and T are within $1\,\%$ of target at gauge wg1 (inlet) and drift to a $5\,\%$ period deviation at wg5 owing to residual reflection from the absorbing outlet.

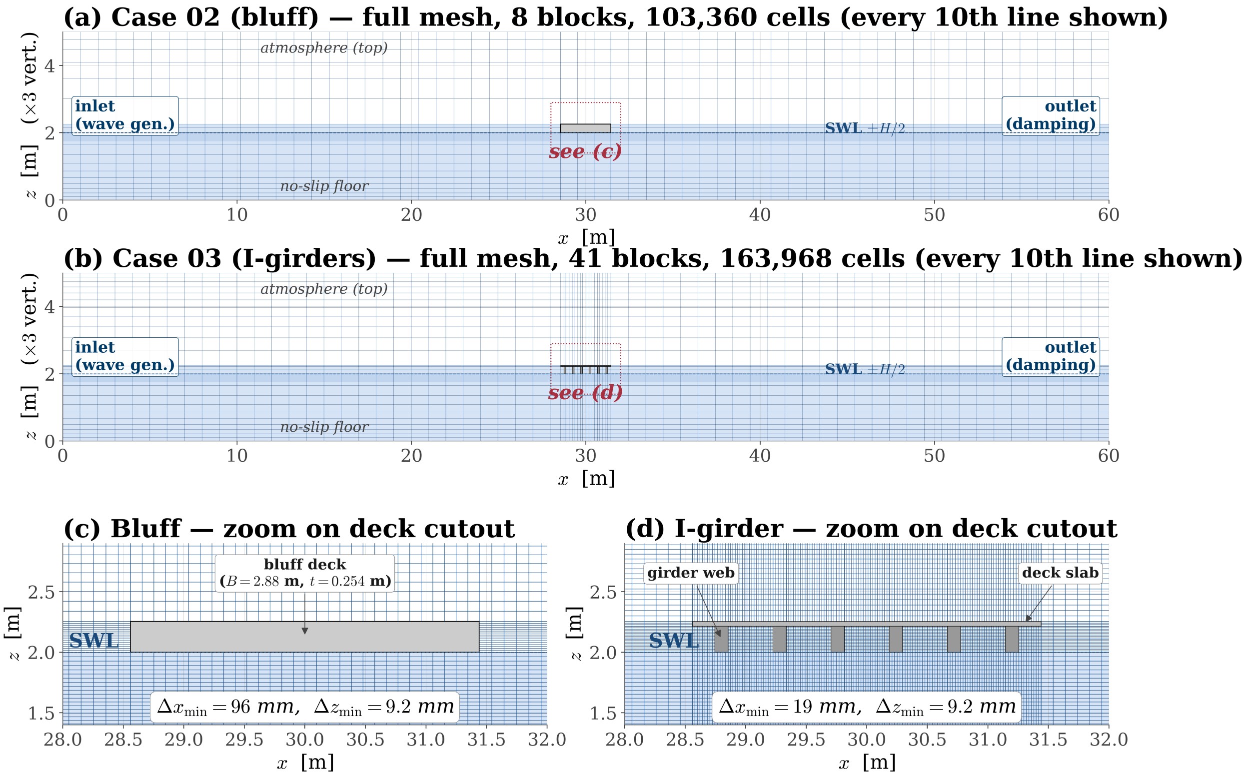

FIG. 3. Deck-region meshes drawn cell-by-cell from the `blockMeshDict` definition. (a) Case 02 bluff full-tank mesh (8 blocks, 103 360 cells; every tenth grid line shown) with the 80-cell free-surface band ($1.3 \leq z \leq 2.7$ m, $\Delta z = 17.5$ mm) overlaid. (b) Case 03 I-girder full-tank mesh (41 blocks, 163 968 cells). (c) Bluff deck cutout zoom. (d) I-girder deck cutout zoom showing the missing-block deck cutout and the inter-girder fluid chambers (orange hatch).

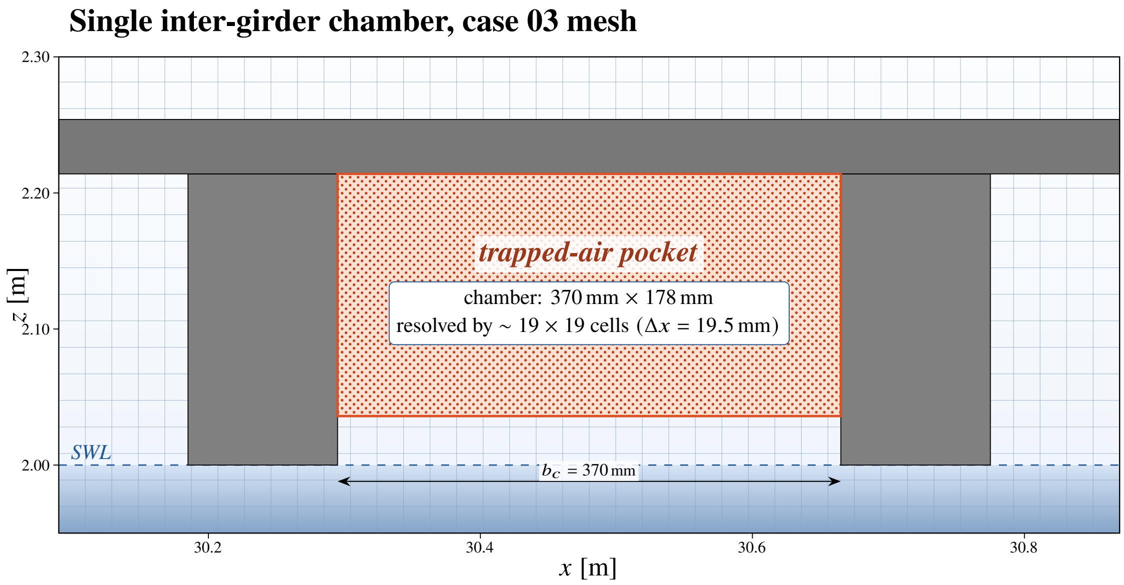

FIG. 4. Inter-girder chamber zoom (case 03) at the chamber cell-grid resolution ($\Delta x = \Delta z = 19.5\,\mathrm{mm}$). Slab and girders are solid (gray); the trapped-air pocket beneath the soffit at the wave-impact instant is crosshatched orange. This is the smallest length scale resolved in the case-03 mesh.

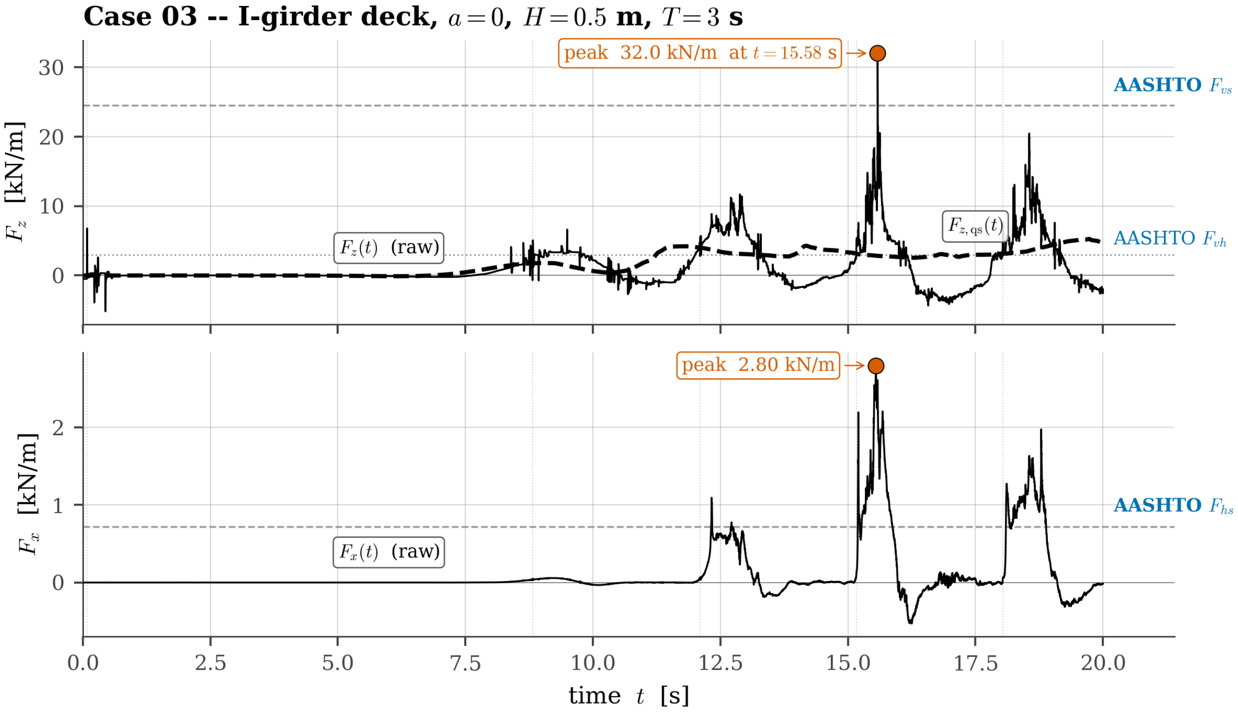

FIG. 5. Case 03 (I-girders): vertical force $F_z(t)$ with AASHTO F_{vs} and F_{vh} references (top), and horizontal force $F_x(t)$ with AASHTO F_{hs} reference (bottom).

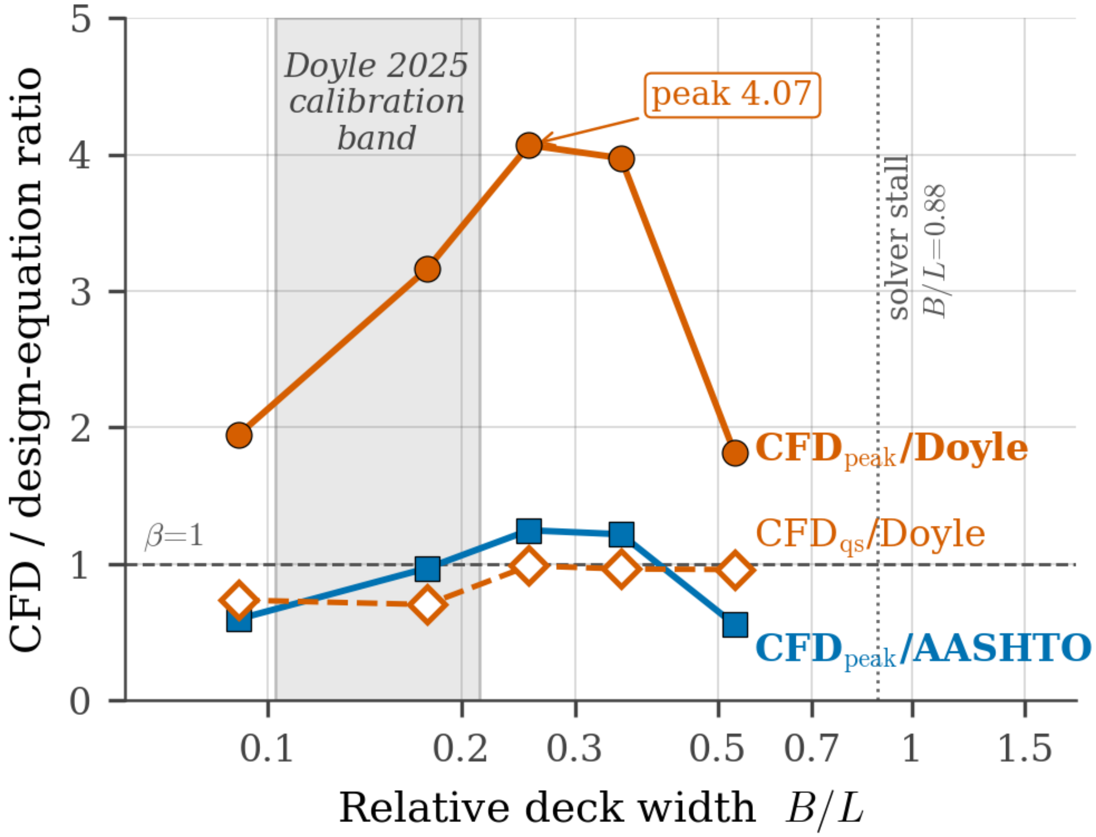

FIG. 6. Bluff-deck geometry sweep (1:5 bluff cross-section, case-02 wave: $H = 0.5\,$m, $T = 3\,$s, $d = 2.0\,$m): CFD-to-design- equation ratio $\beta = F_{\mathrm{CFD}}/F_{\mathrm{design}}$ as a function of relative deck width B/L. Color denotes the denominator equation (vermillion for the modified-Goda formulation of Doyle et al. (2025), also bluff-calibrated; blue for AASHTO 2008); the quasi-static envelope (β_{qs}, open diamonds, dashed) and the peak-basis ratio (β_{peak}, filled markers, solid) are distinguished within each color. The neutral grey band marks the Doyle 2025 calibration range $B/L \in [0.103, 0.213]$; dotted vertical lines mark the two solver stalls at $B/L \geq 0.88$ (Section 6). The peak-basis vermillion trace spikes to $\beta \approx 4$ within the calibration band, but the corresponding quasi-static vermillion trace stays near unity, so the apparent unconservatism is the incompressible slamming-spike artefact rather than a property of the modified-Goda equation.

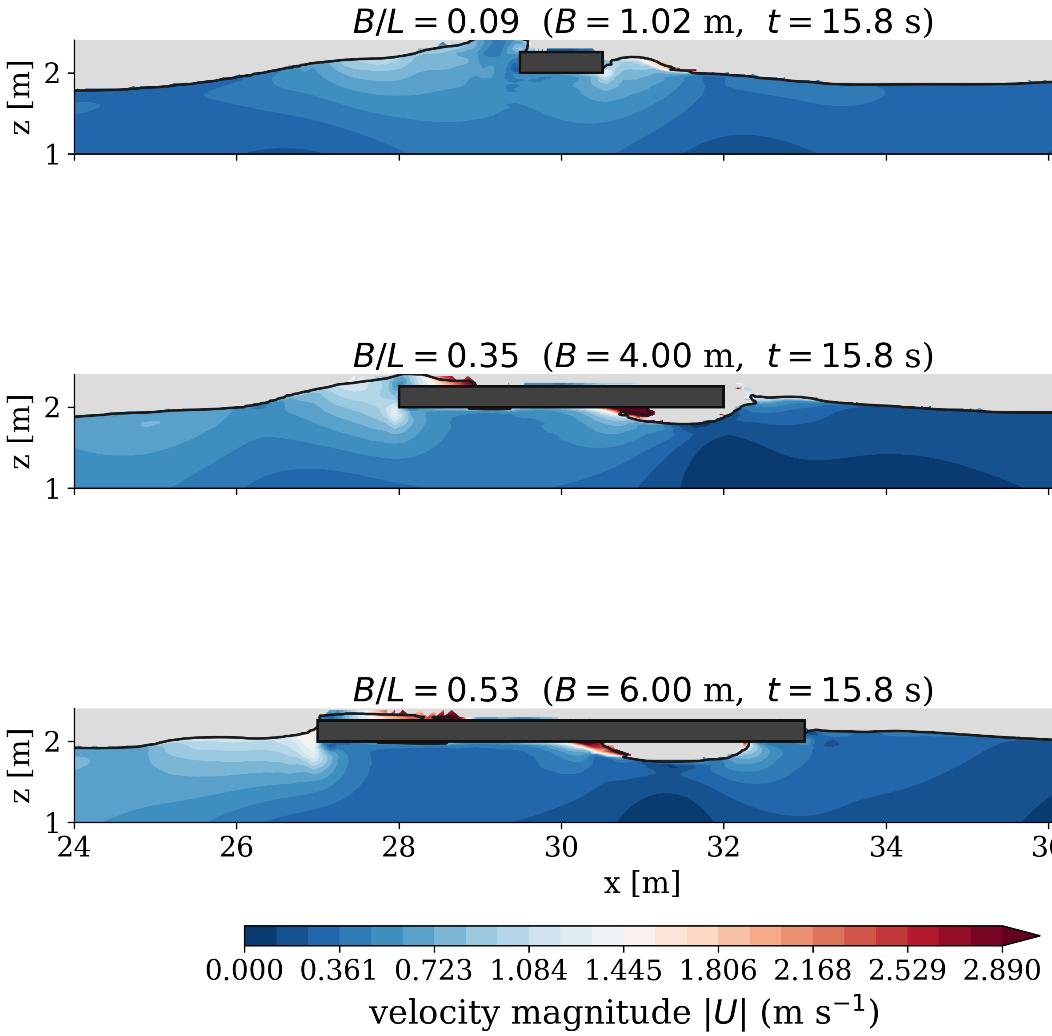

FIG. 7. Flow-field snapshots at $t = 15.8$ s for three deck widths (1:5 bluff cross-section) under the same wave forcing; top to bottom $B/L = 0.09$, 0.35, 0.53. Color is velocity magnitude $|U|$ in the water phase ($\alpha_w \geq 0.3$); air is grey; the black line is the free surface; the yellow region beneath the soffit at $B/L = 0.35$ and 0.53 flags the trapped-air pocket that grows with deck width.

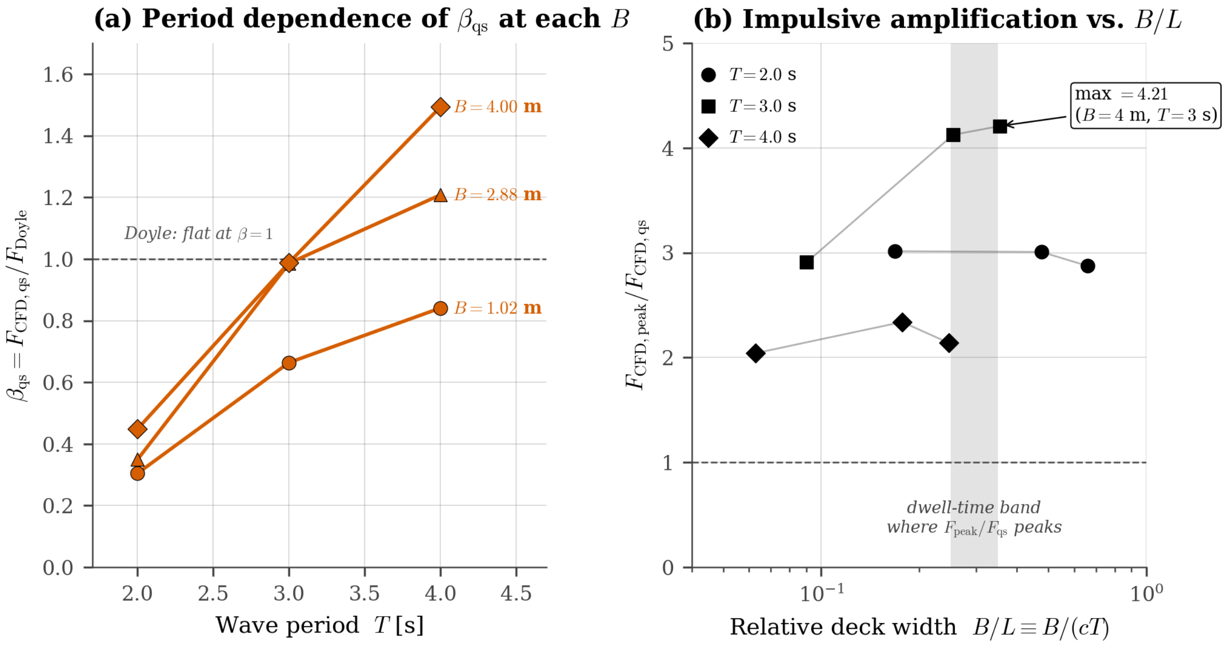

FIG. 8. Bluff-deck cross-product sweep over (B,T) (1:5 bluff cross-section, $H = 0.5$ m, $d = 2.0$ m). (Left) Quasi-static β_{qs} vs. wave period T at each deck width B. Doyle's slender-deck assumption would imply a horizontal line at $\beta = 1$; the CFD shows a factor-of-3 to factor-of-4 variation at every B. (Right) Impulsive amplification F_{peak}/F_{qs} vs. B/L, peaking at the dwell-time-matched corner $(B = 4\,\text{m}, T = 3\,\text{s})$.

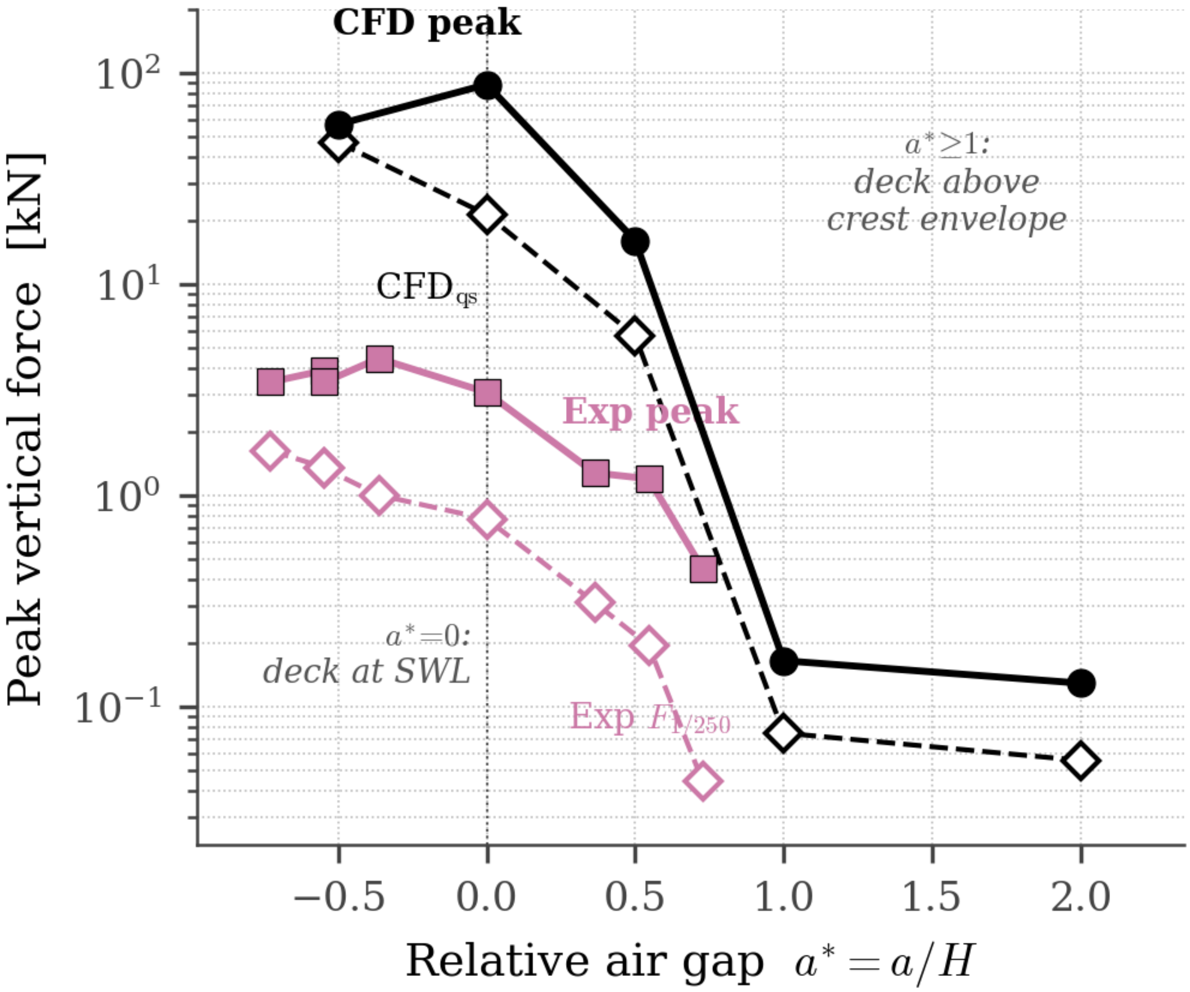

FIG. 9. CFD air-gap sweep (regular Stokes-II $H = 0.5$ m, $T = 3.0$ s, $d = 2.0$ m, 1:5 bluff $B = 2.88$ m) against the PRJ-2131 Test 3 `TMA_X3` experimental sweep ($H_s \approx 0.55$ m, same deck width), on a log vertical scale. Forces are totals over the deck width $B = 2.88$ m. The qualitative shape matches across the full sweep; the impact-spike over-prediction by incompressible `interFoam` at small $|a^*|$ is a multiplicative offset rather than a shape distortion.

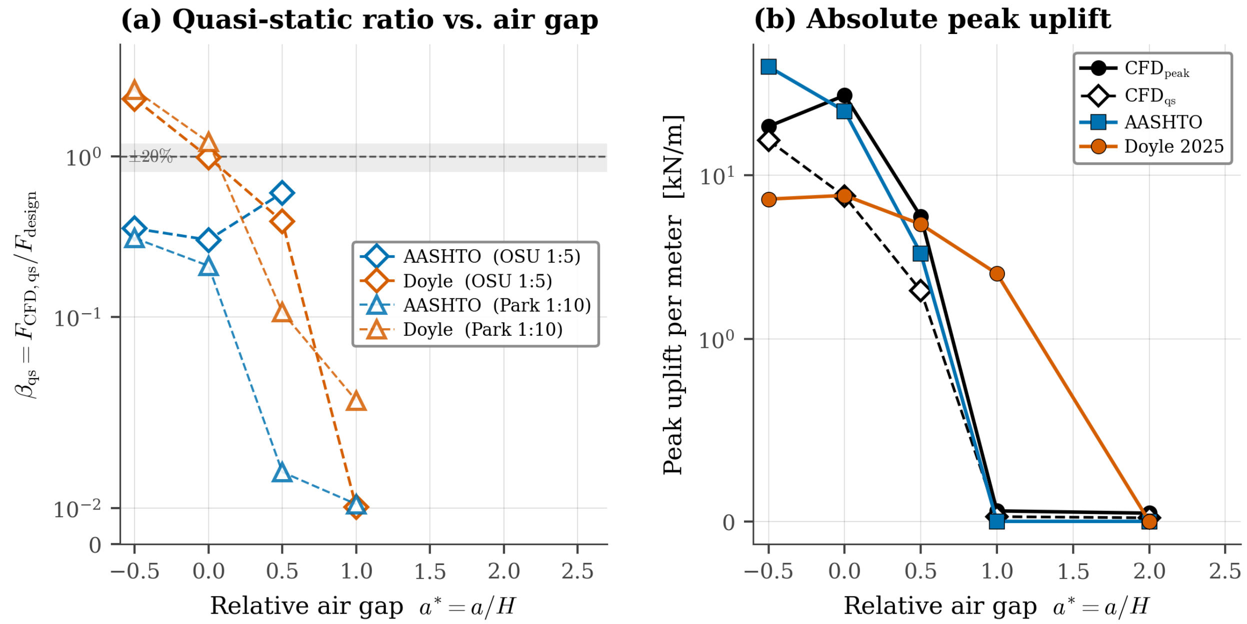

FIG. 10. Design-equation error map for the bluff-deck air-gap sweep (all specimens bluff). (a) CFD-to-design quasi-static ratio $\beta_{qs} = F_{CFD,qs}/F_{design}$ against $a^* = a/H$, with a $\pm 20\,\%$ band shaded as a visual reference; open diamonds are the OSU 1:5 bluff specimen at the case-02 wave ($H = 0.5$ m, $T = 3.0$ s, $d = 2.0$ m), open triangles the Park 1:10 bluff specimen at the X1 design wave ($H = 0.18$ m, $T = 3.72$ s, $d_{local} = 0.40$ m). (b) Absolute peak uplift on the OSU 1:5 bluff specimen at the case-02 wave, with the AASHTO and Doyle predictions overlaid.

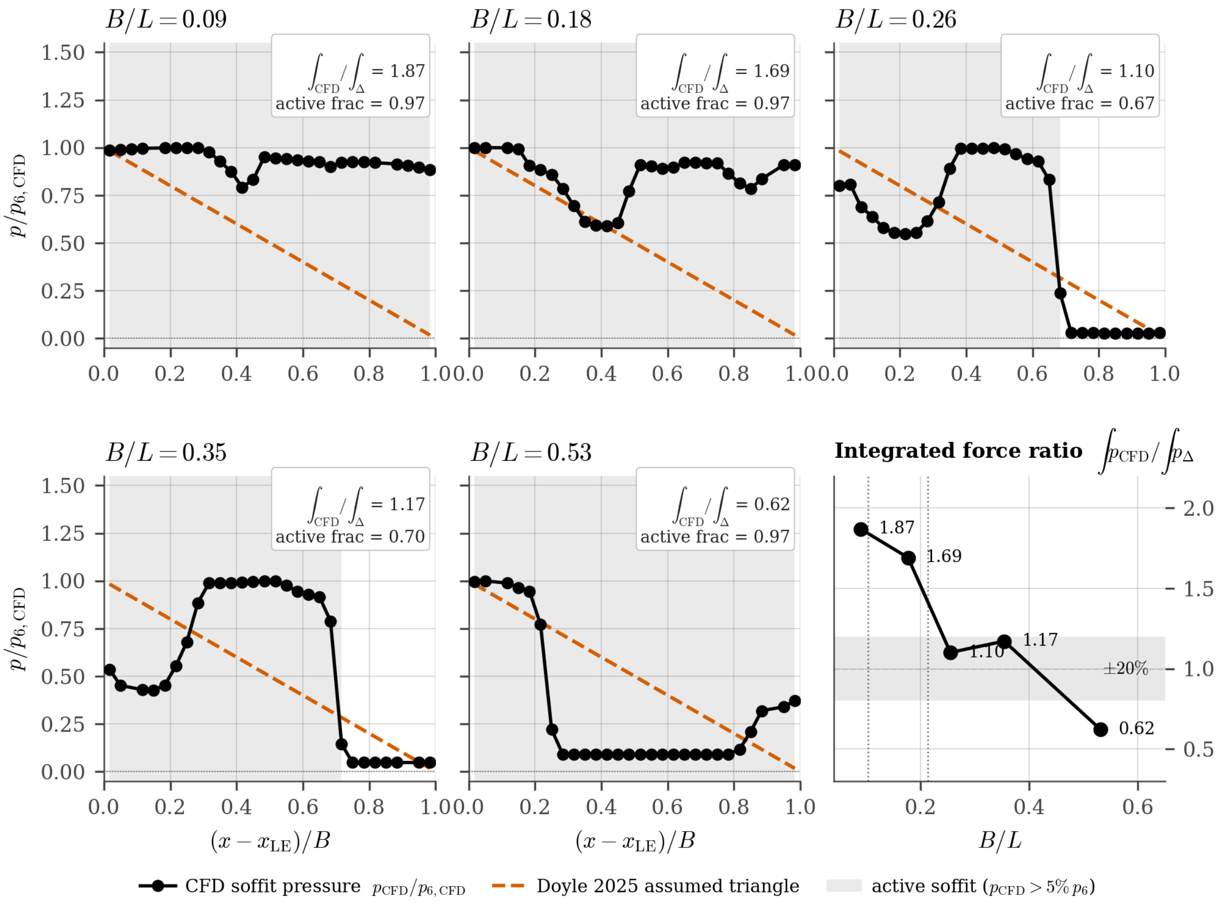

FIG. 11. Soffit pressure distribution at the instant of peak $|F_x|$ for the five well-behaved cases of the bluff geometry sweep, normalized by the leading-edge CFD pressure $p_{6,\text{CFD}}$. Black filled circles trace the CFD-resolved bluff pressure; the dashed vermillion line is the Doyle 2025 triangular assumption (itself derived from a bluff-deck calibration), so the comparison is on matched geometry. The grey shading marks the *active* soffit region where $p_{\text{CFD}} > 5\% \, p_6$. Each panel reports the integral ratio $\int p_{\text{CFD}} / \int p_{\Delta}$ and the active-fraction f_a. The sixth panel plots the integral ratio against B/L with a $\pm 20\%$ band shaded as a visual reference.